

Design of New Concept Direct Grid-Connected Slip-Synchronous Permanent-Magnet Wind Generator

Johannes H. J. Potgieter, *Student Member, IEEE*, and Maarten J. Kamper, *Senior Member, IEEE*

Abstract—This paper deals with the modeling, the design, and the construction of a new concept slip-synchronous permanent-magnet (PM) wind generator for direct-drive direct grid connection. This generator is a variation of the conventional PM induction generator concept as proposed and analyzed in literature. The use of nonoverlap windings is proposed for the first time for this type of generator. Combined analytical and finite-element calculation and design-optimization methods are developed and used in the design of the generator. Load torque ripple and no-load cogging torque are identified as very important design parameters and are minimized to an absolute minimum in the design optimization. The modeling and the design are verified with measurements on a 15-kW prototype wind generator system.

Index Terms—Design optimization, direct grid connection, finite-element (FE) methods, induction generators, modeling, permanent-magnet (PM) machines, slip generators, synchronous generators, wind power generation.

I. INTRODUCTION

THE IDEA of a slip-synchronous permanent-magnet generator (SS-PMG) is based upon the concept of the permanent-magnet induction generator (PMIG). Although the PMIG concept is not overly well known, it was originally proposed in 1926 by [1]. The PMIG makes use of an additional free-rotating permanent-magnet (PM) rotor in the inside of the cage rotor as in Fig. 1(a) or between the stator and the cage rotor of an induction machine as in Fig. 1(b) or outside of the stator, as shown in Fig. 1(c). The PM rotor supplies the magnetic flux within the machine and induces a voltage in the stator winding, as shown in the equivalent circuit of Fig. 2. This, in principle, reduces the magnetizing current and improves the power factor of the machine. The idea proposed in [1] was followed by [2] in 1959 and [3] in 1967 using PM material. In 1992, Low and Schofield [4] used high-energy product PMs for the first

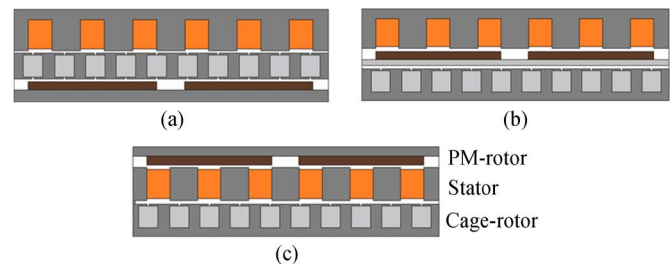


Fig. 1. Different PMIG configurations with (a) cage rotor between PM rotor and stator, (b) PM rotor between cage rotor and stator, and (c) stator between cage rotor and PM rotor.

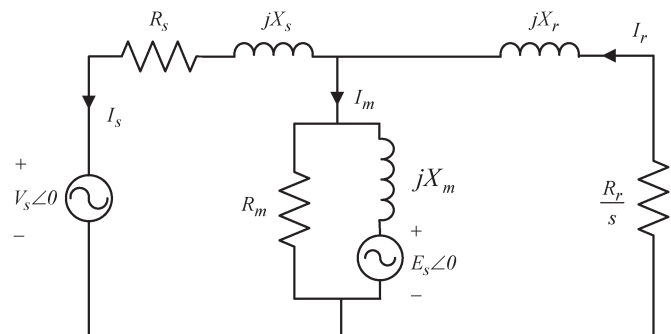


Fig. 2. Equivalent circuit of a conventional PMIG.

time. Recently, the design of the PMIG for large (2-MW) wind turbines was investigated by [5]–[8]. Other recent research works were done in Japan [9], [10] and also by [11]–[13]. Another variation of the concept is proposed in [14], where the PMIG concept is implemented in a gearless doubly fed wind generator system. Also, recently, the use of PMIGs in solid-state converter (SSC) fed wind farms with high-voltage direct-current transmission [15] was investigated. The application is clearly for generators in renewable energy systems.

In all the literature, hitherto, the design and the modeling of this type of generator are based on the conventional PMIG layout as in Fig. 1, using standard stator and cage-rotor windings. Furthermore, experimental testing was done on only low-pole-number machines. Nothing has been reported in the literature about the cogging effect between the PM rotor and the stator or slip rotor, as well as the effect of the load torque ripple on the stability of the PM-rotor. Cogging causes the PM rotor to lock with the stator, and rotor teeth and load torque ripple could further destabilize the machine's operation. Furthermore, transient dq -axis modeling of this type of generator is lacking in literature.

Manuscript received September 15, 2011; revised December 22, 2011; accepted January 8, 2012. Date of publication March 16, 2012; date of current version May 15, 2012. Paper 2011-EMC-439.R1, presented at the 2010 IEEE Energy Conversion Congress and Exposition, Atlanta, GA, September 12–16, and approved for publication in the IEEE TRANSACTIONS ON INDUSTRY APPLICATIONS by the Electric Machines Committee of the IEEE Industry Applications Society.

The authors are with the Department of Electrical and Electronic Engineering, University of Stellenbosch, Stellenbosch 7600, South Africa (e-mail: jpot@sun.ac.za; kamper@sun.ac.za).

Color versions of one or more of the figures in this paper are available online at <http://ieeexplore.ieee.org>.

Digital Object Identifier 10.1109/TIA.2012.2191251

As PMIG-type systems are direct-drive and directly grid connected, they are very attractive for wind generator applications as the use of gearboxes and the use of power electronic converters for grid connection are avoided. In [16], [17], and [18], interesting methods are proposed to connect PM synchronous generator (PMSG) systems to the grid directly. In [16], a spring and damper system is used to damp power angle oscillations of a directly grid-connected PMSG instead of using damper windings, usually incorporated within grid-connected synchronous machines. In [17], a PMSG is connected to a turbine via a hydrodynamically controlled variable speed gearbox, with a fixed speed output. Insight is also given on the low-voltage ride-through (LVRT) capability of the directly grid-connected PMSG in wind farms. Quite recently in [18], a directly grid-connected PMSG is proposed where the active damping of the generator is done by means of a series converter connected in its star point. The converter, however, is rated only 20% of the rated generator power. However, no clarity could be obtained from literature on the feasibility of these direct online PMSG concepts.

In spite of the mentioned advantages and all the research done on direct-drive direct-online systems, not a single wind generator of this type has been installed and tested in practice up to now as far as the authors know. For the PMIG type of systems, the main reason for this is probably the apparently difficult construction. However, with the system proposed in this paper, the construction issues are mitigated to a large extent. Another aspect is the extra set of bearings used in the PMIG type of systems, which normally receives negative comments. The extra set of bearings however operates only at slip speed, and the bearings are also far fewer than the number of bearings used in a gearbox system. Other limiting factors of using direct-online generators can also be the fixed speed disadvantage, the stability of the generator under low-voltage conditions, and the ability to control reactive power. The apparent fixed speed disadvantage should be measured in the predicted per unit energy cost of the system, which includes the installation and the predicted maintenance costs of such a system versus variable speed systems. The LVRT capabilities of directly grid-connected PM generators still need to be investigated in much more detail, but as mentioned in [17], depending on the grid characteristics, it is possible for the generator to continue operation during low-voltage conditions. Reactive power control is also possible as further referred to in this paper.

With PMIG-type systems, there are no disadvantage with regard to efficiency. The machine can be considered as two PM machines in tandem, thus multiplying two efficiencies. However, a normal PM direct-drive generator with an SSC also has two converter actions in tandem and so does the double-fed induction generator plus the gearbox system.

The new approach followed in this paper is validated by the analysis, the design, and the construction of a 15-kW prototype SS-PMG wind turbine system.

II. NEW CONCEPT SS-PMG

The SS-PMG concept as presented in this paper and as shown in Fig. 3(a) and (b) consists of two PM machine units.

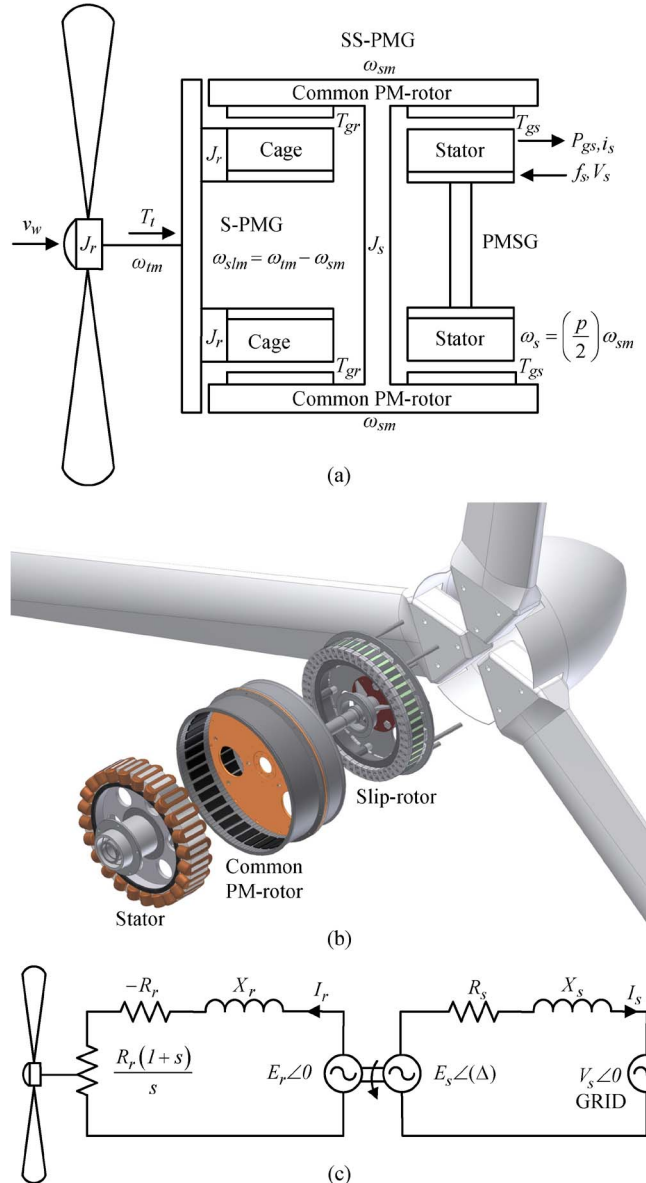


Fig. 3. (a) Cross-sectional diagram, (b) example, and (c) equivalent circuit of a new concept SS-PMG.

It differs from the conventional PMIG system in which the two machine units are magnetically separated. The two machine units are mechanically linked by a common PM rotor. The one generator unit is a normal PMSG with its stationary stator connected to the grid. The other generator operates on a principle similar to that of an induction generator; its short-circuited rotor is mechanically connected to the turbine and runs at slip speed with respect to the synchronously rotating PM rotor. This machine unit is referred to in this paper as a slip PM generator (S-PMG). To the knowledge of the authors, no concept such as the SS-PMG has been reported in literature.

The magnetically split SS-PMG can be thus modeled as two separate decoupled machines, as shown in the per-phase equivalent circuit of Fig. 3(c). The per-phase induced voltages in both machines are due to the rotating PM rotor; in the case of the PMSG, a voltage is induced in the stator

at grid frequency, and in the case of the S-PMG, a voltage is induced at the slip frequency. Note that the S-PMG rotor circuit in Fig. 3(c) is referred to the grid frequency, and the slip and the slip speed are taken as positive in the generator mode. Power transfer thus takes place from the turbine to the slip rotor and then via the PM-rotor to the stator and the grid.

Comments on the SS-PMG versus the conventional coupled PMIG of Fig. 1 are the given below.

- 1) The amount of the PM material used in the SS-PMG is the same as in the PMIG.
- 2) The yoke mass of the SS-PMG will be higher, but this increase will be small in high-pole-number machines relative to the total mass.
- 3) The number of poles and the size of the two machine units in a SS-PMG can differ, which is advantageous from a design point of view; also, for a S-PMG with a higher pole number than the PMSG unit, the yoke mass of the S-PMG will be substantially smaller than that of the PMSG. These design aspects are not possible in a conventional PMIG.
- 4) With a SS-PMG, nonoverlap windings can be used in both the PMSG and the S-PMG, which is a huge advantage in terms of the reduced cogging and load torque ripple and a lower number of coils; a low cogging torque and load torque ripple cannot be overemphasized as they affect the startup of the SS-PMG and the stability of the freely rotating PM rotor.
- 5) In a SS-PMG with the two machine units mounted in tandem, as shown in Fig. 3(b), the air gap diameters of both the S-PMG and PMSG units can be put to a maximum to maximize the generated torque.
- 6) The modularity and the simplicity of the system are largely improved due to the two units independently operating of one another; for example, the S-PMG part of the generator can be completely removed, and the turbine can be directly mounted on the PMSG unit's mounting plate, then resulting in a normal PM wind generator connected to the grid via an SSC.

The mechanical construction of a small (15-kW) SS-PMG wind generator proposed and investigated in this paper is shown in Fig. 3(b). The PM rotor of the S-PMG is mechanically fixed to the PM-rotor of the PMSG, while the rotor winding and core of the S-PMG are mounted onto the turbine mounting plate.

III. STEADY-STATE SS-PMG MODELING

Both the design optimization and the performance evaluation of the SS-PMG are done with the machine in the steady state and with the dq -reference frame fixed to the PM rotor. The dq -equivalent circuits and vector diagrams of the S-PMG and PMSG are shown in Fig. 4(a) and (b), respectively.

A. Equivalent Circuit dq -Modeling

From Fig. 4, the steady-state dq -equations of the short-circuited S-PMG and grid-connected PMSG units are given

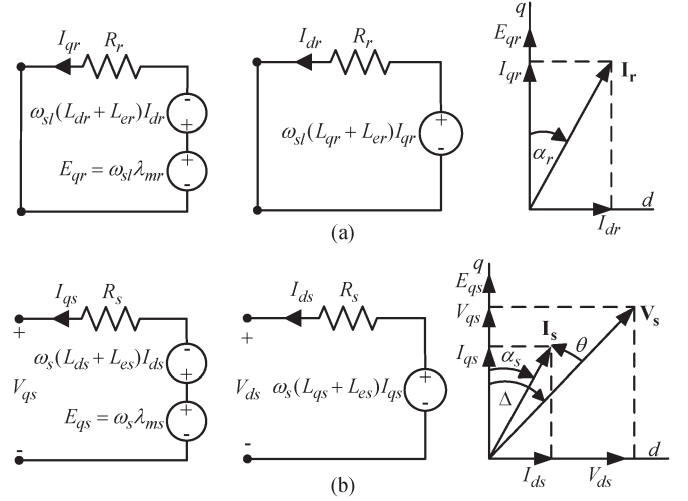


Fig. 4. Steady-state dq -equivalent circuits and vector diagrams of (a) the S-PMG and (b) the PMSG.

respectively by (positive current is taken as flowing out)

$$0 = -R_r I_{qr} - \omega_{sl}(L_{dr} + L_{er})I_{dr} + \omega_{sl}\lambda_{mr} \quad (1)$$

$$0 = -R_r I_{dr} + \omega_{sl}(L_{qr} + L_{er})I_{qr} \quad (2)$$

$$V_{qs} = -R_s I_{qs} - \omega_s(L_{ds} + L_{es})I_{ds} + \omega_s\lambda_{ms} \quad (3)$$

$$V_{ds} = -R_s I_{ds} + \omega_s(L_{qs} + L_{es})I_{qs} \quad (4)$$

where ω_{sl} is the electrical slip speed equal to $\omega_{sl} = \omega_t - \omega_s$, with ω_t being the electrical turbine speed and $\omega_s = 2\pi f_s$ being the synchronous electrical speed, and subscript “ r ” donates the S-PMG slip rotor and “ s ” donates the PMSG stator. The load angle Δ , the current angle α , and the SG's power factor angle $\theta = \Delta - \alpha$ are all defined in the vector diagrams of Fig. 4. The dq -inductances in (1)–(4) and Fig. 4 are defined as

$$L_q = \frac{\lambda_q}{-I_q} \quad L_d = \frac{\lambda_d - \lambda_m}{-I_d}. \quad (5)$$

The per-phase end-winding inductances are indicated by L_{er} and L_{es} in (1)–(4) and Fig. 4 and can be either calculated by analytical methods or finite-element (FE) analysis. If surface-mounted PMs are used, then usually, $L_d = L_q$. However, this was found not to be the case as further considered in Section VII. The general relations of voltage, current, and copper losses are given by (6)–(9) as

$$\begin{bmatrix} V_{qs} \\ V_{ds} \end{bmatrix} = \sqrt{2}V_{\text{rms}} \begin{bmatrix} \cos \Delta \\ \sin \Delta \end{bmatrix} \quad (6)$$

$$\begin{bmatrix} I_q \\ I_d \end{bmatrix} = \sqrt{2}I_{\text{rms}} \begin{bmatrix} \cos \alpha \\ \sin \alpha \end{bmatrix} \quad (7)$$

$$V_{qs}^2 + V_{ds}^2 = 2V_{\text{rms}}^2 \quad (8)$$

$$I_q^2 + I_d^2 = 2I_{\text{rms}}^2 \quad (9)$$

$$I_{\text{rms}}^2 = \frac{P_{\text{cu}}}{3R} \quad (10)$$

with P_{cu} in (9) being the copper loss of the slip rotor or stator winding. V_{rms} in (7) indicates the fixed grid voltage.

B. Performance Modeling

The developed torques of both the S-PMG and the PMSG are, in general, expressed by

$$T_g = \frac{3}{4}p[(L_q - L_d)I_d I_q + \lambda_m I_q]. \quad (10)$$

The efficiency of the SS-PMG is given by

$$\eta = \eta_s \eta_r \quad (11)$$

where

$$\eta_r = \frac{P_{gr}}{P_t} = \frac{T_{gr}\omega_{sm}}{T_{gr}\omega_{tm}} = 1 - s \quad (12)$$

$$\eta_s = \frac{P_{gs}}{P_{gr}} = \frac{T_{gr}\omega_{sm} - (P_{ecs} + P_{wfs}) - P_{cus}}{T_{gr}\omega_{sm}} \quad (13)$$

and where subscript “ m ” donates mechanical speed. In (13), P_{wfs} and P_{ecs} are the wind-and-friction and the eddy-current-and-core losses of the PMSG, respectively. Note that P_{wfr} and P_{ecr} of the S-PMG are practically zero; thus, from (12), the only remaining (copper) losses are given by $P_{cur} = T_{gr}\omega_{slm}$. The torque of the PMSG is also given from (13) by

$$T_{gs} = T_{gr} - \frac{P_{ecs} + P_{wfs}}{\omega_{sm}}. \quad (14)$$

P_{ecs} in (13) and (14) includes the eddy-current losses in the magnets and the PM yoke of the PMSG, which can be substantial when using solid magnets and solid rotor yokes [19], [20]. With the generator operating at a constant speed, P_{wfs} is considered as constant in the modeling and is determined once. The stator-core losses of the PMSG are calculated by means of an empirical formula using, among other things, the air gap flux density data from the FE analysis. The PMSG’s eddy-current losses in the magnets and the PM yoke are also determined once from FE transient loss calculations of the optimum designed machine.

Finally, the PMSG’s working power and reactive power supplying to or consuming from the grid are given by

$$\begin{bmatrix} P_{gs} \\ Q_{gs} \end{bmatrix} = 3V_{rms}I_{rms} \begin{bmatrix} \cos \theta \\ \sin \theta^* \end{bmatrix}. \quad (15)$$

IV. STEADY-STATE FE SIMULATION

Unlike a converter-fed PMSG wind generator system where the PMSG is under current control by using an SSC, the grid-connected SS-PMG is an uncontrolled system. The current state of the SS-PMG for each load, thus, is unknown. Instead of using transient FE (T-FE) analysis that takes time, a number of nonlinear static FE (S-FE) solutions are used to simulate the state of the SS-PMG. Knowing the state of the SS-PMG, the performance of the SS-PMG can be calculated, as explained earlier. This simulation method is also needed and used in the design optimization of the SS-PMG, as explained in the next section.

A. Rewriting the Steady-State Equations

In order to simulate the performance of the machine, the steady-state equations of the SS-PMG given in Section III-A need to be solved first. With these solved, the performance of the machine can be calculated by using the performance equations in Section III-B. To explain the solving process more clearly, (1)–(8) are rewritten as follows:

For the S-PMG from (2),

$$I_{qr} = \frac{R_r}{\omega_{sl}(L_{qr} + L_{er})} I_{dr}. \quad (16)$$

Substitute (16) in (1) to obtain

$$\omega_{sl}^2 = \frac{I_{dr}R_r^2}{(L_{qr} + L_{er})(\lambda_{mr} - (L_{dr} + L_{er})I_{dr})}. \quad (17)$$

Substitute (16) also in (8), which gives

$$\omega_{sl}^2 = -\frac{R_r^2 I_{dr}^2}{I_{dr}^2 (L_{qr} + L_{er})^2 - 2I_{rms}^2 (L_{qr} + L_{er})^2}. \quad (18)$$

Set (17) = (18), resulting in a second-order polynomial, which can be solved for I_{dr} as

$$I_{dr}^2 (L_{qr} - L_{dr}) + I_{dr} \lambda_{mr} - 2I_{rms}^2 (L_{qr} - L_{er}) = 0. \quad (19)$$

With (19) solved, I_{dr} can be substituted in (16) and (17) to calculate I_{qr} and ω_{sl} , and hence α_r from (6).

The steady-state dq -equations of Section III-A can be also used to solve the unknowns of the PMSG unit, except that, in this case, there are more variables, which complicates the calculations. However, to simplify the calculations, a slightly different approach is followed by solving V_{ds} and V_{qs} separately, as explained in the next section.

The equations used to solve for the unknowns of the PMSG are obtained by first rewriting (4) with the result given in (20) as

$$I_{qs} = \frac{V_{ds} + I_{ds}R_s}{\omega_s(L_{qs} + L_{es})}. \quad (20)$$

By substituting (20) into (3), the result is (21) given as

$$I_{ds} = \frac{\omega_s(L_{qs} + L_{es})(\omega_s \lambda_{ms} - V_{qs}) - V_{ds}R_s}{R_s^2 + \omega_s^2 L_{ds}L_{qs}L_{es}^2}. \quad (21)$$

If V_{ds} and V_{qs} are known, I_{ds} can be calculated from (21) and I_{qs} from (20), and hence, α_s can be calculated from (6).

B. Simulation Procedure Method

To calculate and evaluate the performance of the machine, several steps are used, as also described in Fig. 5.

- 1) I_{rms} is calculated from (9) at the rated given copper losses and with R analytically calculated according to the given slot dimensions.

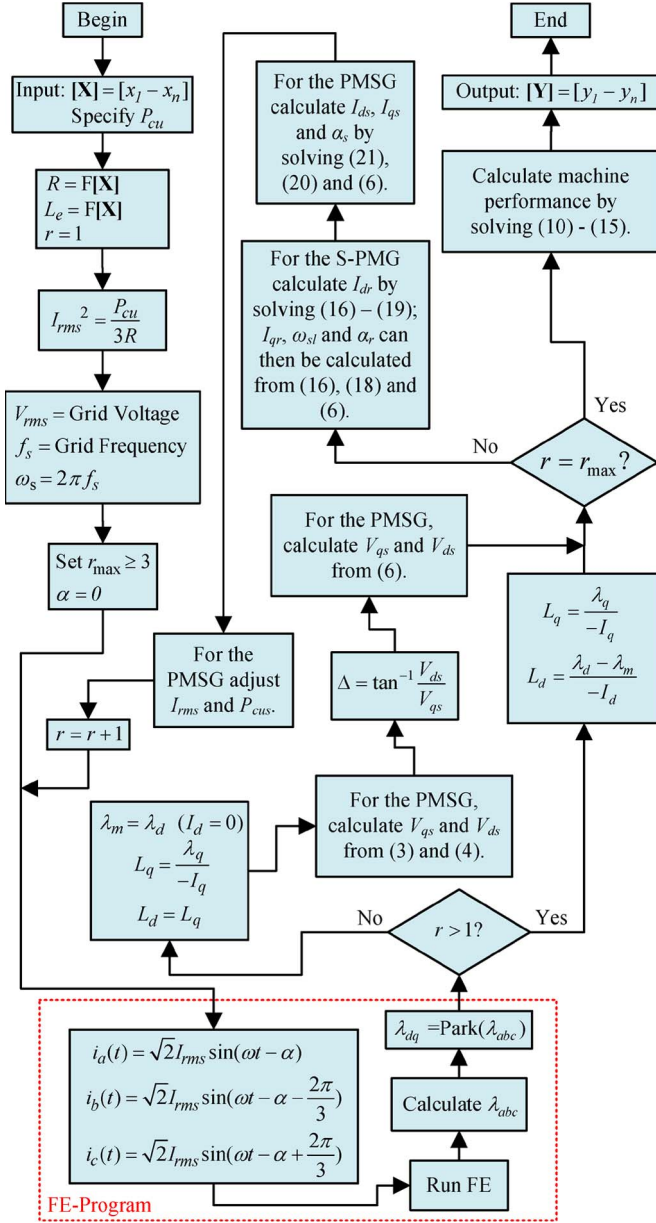


Fig. 5. FE simulation method used to calculate SS-PMG performance (PMSG and S-PMG units separately analyzed).

2) The three phase currents can be then written as

$$\begin{aligned} i_a(t) &= \sqrt{2}I_{\text{rms}} \sin(\omega t - \alpha) \\ i_b(t) &= \sqrt{2}I_{\text{rms}} \sin\left(\omega t - \alpha - \frac{2\pi}{3}\right) \\ i_c(t) &= \sqrt{2}I_{\text{rms}} \sin\left(\omega t - \alpha + \frac{2\pi}{3}\right). \end{aligned} \quad (22)$$

3) With I_{rms} known, α is set to zero in (22), and a first FE iteration is run.

4) λ_{dq} can be then calculated from this first FE iteration, i.e., by transforming the FE-calculated phase flux linkages (λ_{abc}) to dq -parameters using Park's transformation. In this way, the effect of the q -axis current I_q on λ_m is

taken into account; thus, with $\alpha = 0$ and $I_d = 0$, it can be assumed that $\lambda_m = \lambda_d$.

- 5) Also, at this first iteration, it is assumed that $L_d = L_q$ with L_q calculated as in (5) with $I_q = \sqrt{2}I_{\text{rms}}$ in this case. The end-winding inductance L_e can be calculated from separate FE analysis or analytically.
- 6) For the S-PMG, with L_{dr} , L_{qr} , L_{er} , and λ_{mr} known, (19) can be solved for I_{dr} and I_{qr} , and ω_{sl} and α_r can be calculated from (16), (17), and (6), respectively, as mentioned.
- 7) For the PMSG to solve (21) for I_{ds} , values for V_{ds} and V_{qs} are needed. With $I_{ds} = 0$ and $I_{qs} = \sqrt{2}I_{\text{rms}}$ for this first iteration, (3) and (4) can be solved for V_{qs} and V_{ds} . From the vector diagram in Fig. 4(b)

$$\Delta = \tan^{-1} \frac{V_{ds}}{V_{qs}} \quad (23)$$

which gives an approximate value for Δ . With Δ known, V_{qs} and V_{ds} are again calculated except that, in this case, by solving (6) with V_{rms} being the grid voltage. I_{ds} , I_{qs} , and α_s can be now calculated from (21), (20), and (6), respectively.

- 8) With an initial value for α known, another S-FE iteration is run with α substituted in (22). For the S-PMG, the same I_{rms} as previously calculated from (9) is used. However, for the PMSG, because I_{ds} and I_{qs} were not calculated in terms of I_{rms} , a new value for I_{rms} is calculated from (8) and also for P_{cus} from (9).
- 9) New values for L_d and L_q according to (5) are now calculated from the dq -flux linkages with $L_d \neq L_q$ and λ_m as calculated in the first iteration. A new more accurate value for α is obtained by again solving (8), (16), and (6) for the S-PMG and (21), (20), and (6) for the PMSG.
- 10) This new more accurate value for α is then used in a third S-FE iteration, at which point the performance of the machine is evaluated by solving (10)–(15).
- 11) For higher accuracy, more S-FE iterations can be run, but a minimum of three S-FE solutions is required.
- 12) In this simulation procedure, the S-PMG and the PMSG are separately analyzed. For the performance evaluation of the whole SS-PMG system, the performance of both units are evaluated against T_{gr} . With P_{wfr} and P_{ecr} equal to zero, from Fig. 3(a), $T_{gr} = T_t$. T_{gr} is thus the mechanical torque input for the simulation of both machine units.
- 13) To calculate the machine performance at different loads, the simulation procedure can be run with P_{cu} being a variable input parameter for both machine units.

V. FE DESIGN OPTIMIZATION

The design optimization is done by means of an optimization algorithm (Powell's algorithm [21]) that is integrated with the FE program and simulation method, as described in Fig. 5. The design optimization is done in the same manner as described in [22]. Fig. 6 also gives a more diagrammatic view of the design optimization process. In the design optimization of Fig. 6, \mathbf{Y} is the output performance parameter of the machine to be

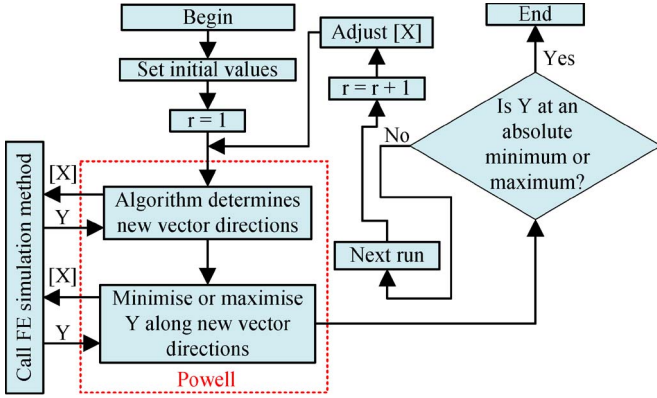


Fig. 6. Optimization process combined with FE simulation method.

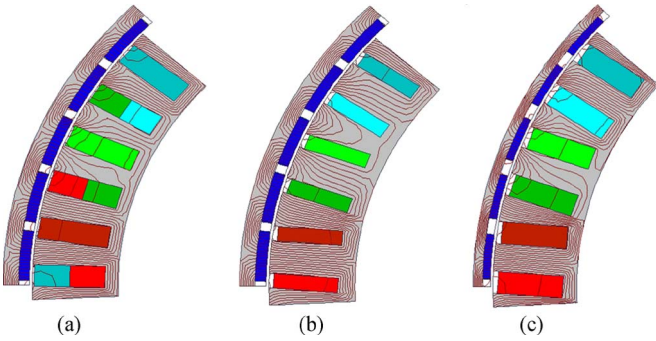


Fig. 7. Cross section and FE plots of (a) DL-S-PMG, (b) SL-S-PMG, and (c) SL PMSG.

maximized or minimized as a function of the multidimensional vector \mathbf{X} . \mathbf{X} includes all the variable machine design parameters. With each iteration r , the optimization algorithm calls the FE program to calculate the function value of \mathbf{Y} for a given \mathbf{X} . The FE program then remeshes the machine structure according to \mathbf{X} and calculates the function value. The design optimization is done by maximizing the torque per given copper losses of the machine. The copper losses are kept constant through the design optimization and are specified according to the thermal capacity and the approximate required efficiency of the machine.

VI. PROTOTYPE S-PMG DESIGN

Maximizing the torque per copper losses at a fixed speed is the same as maximizing the efficiency of the S-PMG, as the core losses of the S-PMG are practically zero. The objective function to be maximized in the optimization, thus, is given by

$$\mathbf{Y} = \mathbf{F}(\mathbf{X}) = \frac{T_{gr}}{P_{cur}}(\mathbf{X}). \quad (24)$$

The cross sections and the FE modeling of the nonoverlap winding S-PMG and PMSG units are shown in Fig. 7. As the grid frequency is 50 Hz and the rated turbine speed is 150 r/min, the number of poles for the PMSG is $p = 40$; the same number of poles is also used for the S-PMG in this case, but it is possible to use a different pole number for the S-PMG unit. With $p = 40$ and choosing the high winding factor 10/12 pole-slot combination, five poles and six slots form a

TABLE I
DIMENSIONS AND PERFORMANCE OF FE OPTIMIZED SS-PMG

Parameter	S-PMG	PMSG
Outer diameter, d_o (mm)	652	653.5
Inner diameter, d_i (mm)	483	497
Magnet pitch / pole pitch, σ_m	0.84	0.73
Air gap (mm)	2	2
Slot width, σ_g (mm)	17.5	18
Slot opening width / Slot width ratio, σ_w (mm)	0.81	1
Yoke height, h_s (mm)	10	10
Magnet-yoke height, h_r (mm)	11.5	7.25
Magnet height, h_m (mm)	8	6
Axial length, l (mm)	62.5	100
Torque (Nm)	1000	1000
Breakdown torque (Nm)	1300	-
Efficiency (%)	98	94
Rated slip (%)	2	-
L_d/L_q at rated load	1.45	1.46

machine section in the FE model using odd periodic boundary conditions.

For both the S-PMG and the PMSG, surface-mounted PMs are used. For the S-PMG, both double-layer (DL) and single-layer (SL) [see Fig. 7(a) and (b)] slip-rotor windings are investigated, but for the PMSG, only a SL winding with preformed coils is considered [see Fig. 7(c)]. In the case of the S-PMG, solid rotor yokes are used instead of laminations, as used for the PMSG unit, as the eddy-current frequencies are very low.

In this paper, the optimum design of only the PM rotor and the slip rotor of the S-PMG shown in Fig. 7(a) and (b) are considered. The design of the PMSG is thoroughly covered in [23]. The design optimization of the 15-kW S-PMG is done subject to the required performance of the machine given by \mathbf{U}_r and \mathbf{G}_r as

$$\mathbf{U}_r = \begin{bmatrix} P_{gr} \\ \omega_{sm} \\ \eta_r \end{bmatrix} = \begin{bmatrix} 16 \text{ kW} \\ 15.71 \text{ rad/s} \\ 98\% \end{bmatrix}$$

$$\mathbf{G}_r = \begin{bmatrix} T_{gr} \\ P_{cur} \\ \omega_{slm} \end{bmatrix} = \begin{bmatrix} 1000 \text{ Nm} \\ 320 \text{ W} \\ 0.314 \text{ rad/s} \end{bmatrix} \quad (25)$$

where $P_{gs} = 15 \text{ kW}$ with $\eta_s = 94\%$ given and where the synchronous speed is 150 r/min. The S-PMG's efficiency is taken very high in (12) to ensure an overall efficiency of $\eta > 92\%$. Note from (25) that the rated slip is 2% and that a lower required efficiency will increase the rated slip.

The machine design parameters to be optimized are given in (26) as

$$\mathbf{X} = \begin{bmatrix} \mathbf{X}_1 \\ \mathbf{X}_2 \end{bmatrix} \quad \mathbf{X}_1 = \begin{bmatrix} \sigma_m \\ \sigma_g \\ \sigma_w \\ h_r \\ h_s \end{bmatrix} \quad \mathbf{X}_2 = \begin{bmatrix} d_0 \\ d_i \\ l \\ h_m \end{bmatrix}. \quad (26)$$

The design parameters given in \mathbf{X} are explained in Table I. To keep the design optimization simple, the outer and inner stack diameters are kept more or less the same as that of the PMSG. After the design optimization, the axial stack length of the S-PMG is adjusted so as to obtain the required performance

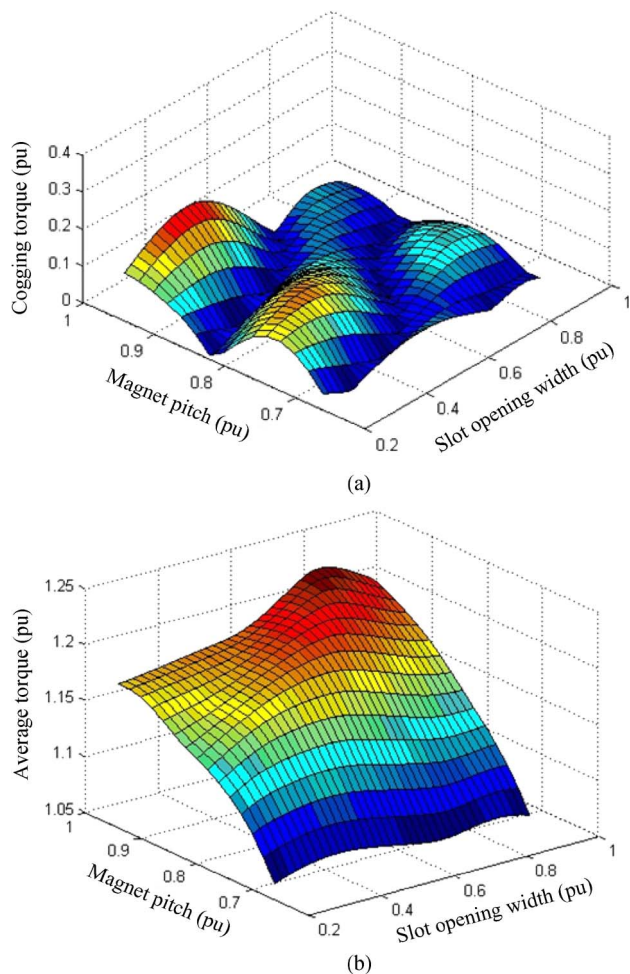


Fig. 8. Sensitivity of (a) cogging torque and (b) average torque to a variation in magnet pitch and slot opening width of the S-PMG, with P_{cur} constant. (values: 1 pu magnet pitch = pole pitch; 1 pu slot opening width = slot width).

of (25) at rated copper losses. At this new axial length, a next design optimization is executed to confirm the optimum design.

After the completion of the optimum design by optimizing the parameters in \mathbf{X}_1 and \mathbf{X}_2 for the maximum torque as previously described, the cogging torque of the S-PMG is next minimized by further adjustments of the parameters included in \mathbf{X}_1 ; these dimensions have the largest effect on the cogging torque. A sensitivity analysis procedure is followed to determine the sensitivity of the cogging torque to magnet pitch and slot opening variations. These results are shown in Fig. 8 and are obtained from a high number of S-FE solutions. The cogging torque is calculated by means of the Maxwell stress tensor method and by position stepping the rotor until a cogging torque cycle is achieved as described in [23]. It is clear from Fig. 8(a) that there are regions where the cogging torque is very low and fairly independent of dimensional change. Shown in Fig. 8(b) is the much less sensitive behavior of the average torque to dimensional changes as opposed to the cogging torque. Also, shown in Fig. 9 is the relatively low sensitivity of the cogging torque to magnet pitch variation, which is fairly independent of slot opening in a certain region.

The final machine dimensions found from the design optimization and the cogging torque minimization are given

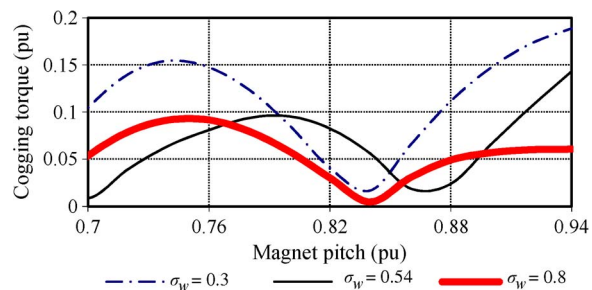
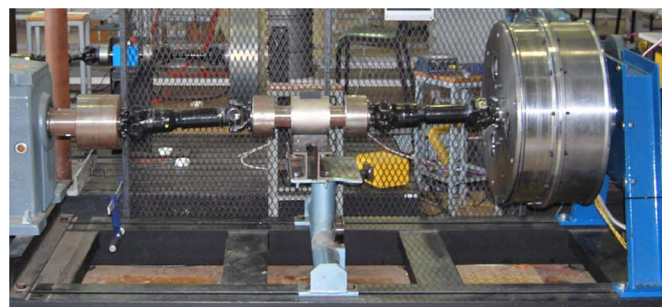
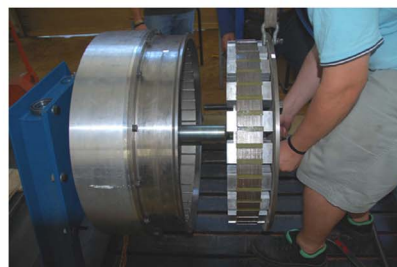


Fig. 9. Sensitivity of cogging torque to magnet pitch variation with slot opening width a parameter of the S-PMG, with P_{cur} constant. (values: 1 pu magnet pitch = pole pitch; 1 pu slot opening width = slot width).



(a)



(b)



(c)



(d)

Fig. 10. (a) (Right) Fifteen-kilowatt SS-PMG wind generator under test via (middle) a torque sensor and (left) a drive system. (b) S-PMG unit fixed to the front of the PMSG unit. (c) DL-S-PMG wound and (d) SL-S-PMG cage slip rotors.

in Table I as for the optimum cross-sectional layout of the S-PMG shown in Fig. 7(a). Also, given in Table I is the rated performance of the S-PMG. At the relatively high efficiency of 98%, the active mass of the optimum designed S-PMG is 65.9% that of the optimum designed PMSG. This is mainly due to the much better filling factor using solid rotor bars.

VII. PERFORMANCE RESULTS

Fig. 10(a) shows the fully assembled SS-PMG system mounted on a test bench in the laboratory. The assembly of the S-PMG unit to the PMSG unit is shown in Fig. 10(b). For

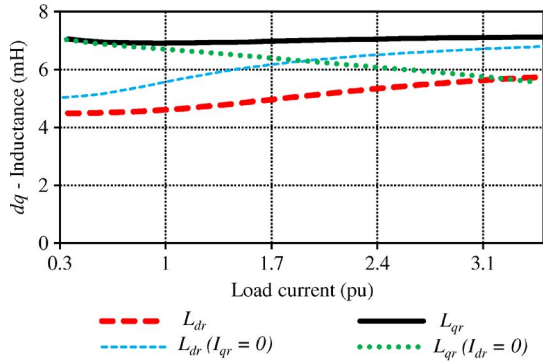


Fig. 11. FE calculated dq -inductances versus load current of the S-PMG.

the practical evaluation of the SS-PMG concept, two different S-PMG units were built, namely, the DL-S-PMG [see Fig. 7(a) and (c)] and the SL-S-PMG [Fig. 7(b) and (d)]. The same SL-PMSG as shown in Fig. 7(c) is used for the evaluation of both S-PMG units.

Due to manufacturing constraints, it was not possible to build the optimally FE designed S-PMG of which the dimensions and FE predicted performance are given in Table I. The connections of the DL-S-PMG make it difficult to use solid bars, and therefore, windings were used instead, as shown in Fig. 10(c), to validate the concept. For the SL-S-PMG, a preformed solid bar winding made from aluminum was used similar to the SL-PMSG windings, as shown in Fig. 10(d). It should be noted that the SL-S-PMG slip rotor was not optimally designed; instead, a basic design iteration was followed to fit the SL slip rotor more or less within the same dimensions as that of the optimally designed DL-S-PMG. Although the conductance of aluminum is poorer than that of copper, it leads to a significant reduction in weight. It is also extremely important to use pure aluminum as the electrical properties of aluminum alloys, as used for the manufacturing of the SL-S-PMG solid bar windings, are significantly different. The poor fill factor of the DL winding and the higher resistance of the aluminum SL coils increase the per-unit resistance, which increases the rated slip value and decreases the efficiency as in (12).

The FE results given in this paper are calculated by means of the S-FE simulation method, as discussed in Section IV. To validate the S-FE results, T-FE analysis is also used to simulate the performance of the S-PMG units.

The variation of the dq -inductances versus load for the DL-S-PMG are shown in Fig. 11. Also, shown in Fig. 11 are the variations of L_{dr} if $I_{qr} = 0$ and of L_{qr} if $I_{dr} = 0$. From these variations, the effects of cross magnetization and saturation, specifically in the PM yoke, are very clear.

Fig. 12 shows the simulated and measured cogging torque of the SL-S-PMG. This measurement is done in the manner described in [23], by varying the rotor in discrete steps and taking the static torque reading at each step. This is a difficult parameter to exactly measure as simulated. Furthermore, as reported in [23], even slight manufacturing deviations can lead to a significant change in the cogging torque results. The torque ripple at rated load of the DL-S-PMG is also shown in Fig. 12. This parameter is even more difficult to accurately measure due

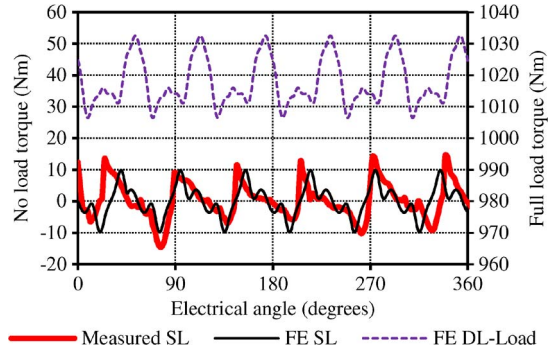


Fig. 12. FE calculated load torque ripple of the DL-S-PMG and no-load torque ripple of the SL-S-PMG versus electrical angle.

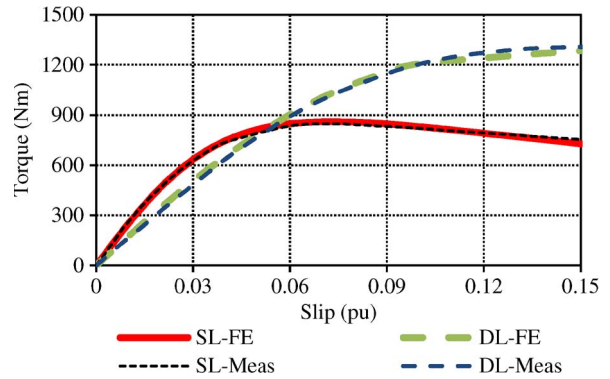


Fig. 13. FE calculated and measured torque versus slip of the DL and SL-S-PMGs.

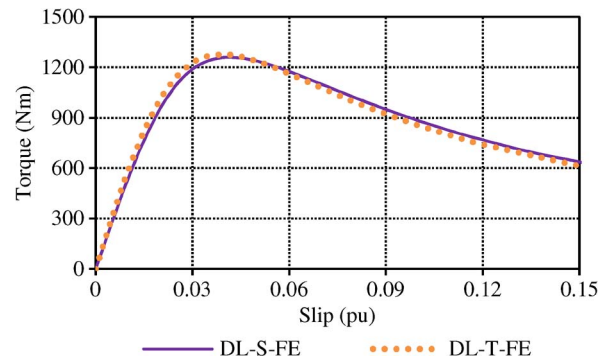


Fig. 14. S-FE versus T-FE analyses of the optimum DL-S-PMG configuration versus slip.

to the several dynamic effects within the drive train setup and is not measured.

Fig. 13 shows the FE simulated and measured torque performance versus the slip of the SL- and DL-S-PMG units. Also, shown in Fig. 14 is the torque of the optimum designed DL-S-PMG as in Table I, with the torque calculated by S-FE and T-FE analyses. With the axial length of the S-PMG very short in comparison with its radial dimension, the end-winding inductance L_{er} has a significant effect on particularly the breakdown torque of the S-PMG units. Care should be also taken with regard to the temperature operating point specified for the magnets in the FE models, as even a slight reduction (e.g., 5%) in the magnet strength has a significant effect on the breakdown torque. Fig. 15 shows the measured efficiencies of

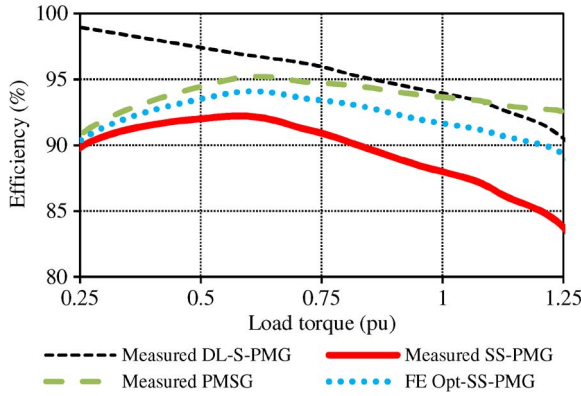


Fig. 15. Measured efficiency versus load of the DL-S-PMG, PMSG, SS-PMG, and FE predicted efficiency of the optimally designed SS-PMG.

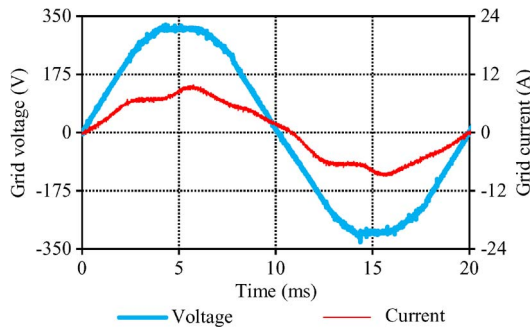


Fig. 16. Load current $i_s(t)$ and line-to-neutral grid voltage $v_s(t)$ waveforms of the SS-PMG versus time at low load, with the rated RMS load current of 23 A.

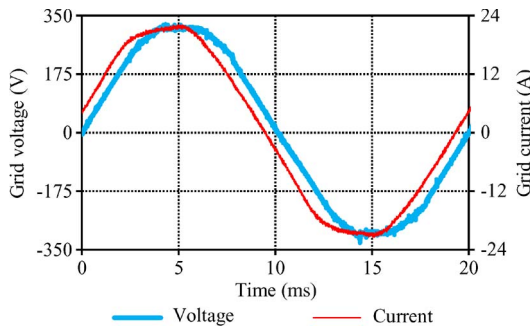


Fig. 17. Load current $i_s(t)$ and line-to-neutral grid voltage $v_s(t)$ waveforms of the SS-PMG versus time at almost full load, with the rated RMS load current of 23 A.

both S-PMG units and the PMSG unit. The efficiency versus the load of the optimum designed SS-PMG as in Table I is also shown.

The measured current waveforms of the directly grid-connected PMSG are shown in Fig. 16 at a very low load and at almost full load in Fig. 17. The variation of the reactive power and the power factor with load is shown in Fig. 18. Fig. 19 shows the reactive power and no-load line current of the PMSG versus grid voltage at zero load. With the active power component of the current almost zero, the current shown in Fig. 19 can be assumed as the reactive current component. This variation in reactive power and current is very interesting as it implies that the generator can be designed to supply, at low loads, capacitive reactive power to the grid but, at high loads, to

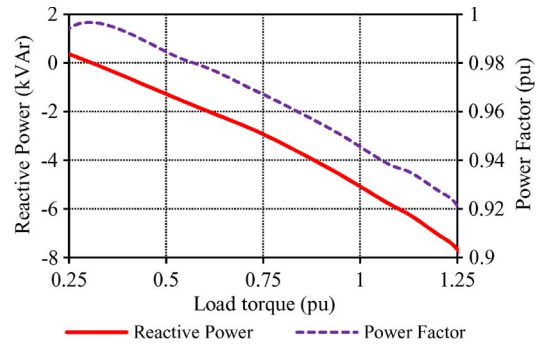


Fig. 18. Measured reactive power and power factor of the SS-PMG versus per-unit load torque ($V_s = 225$ V).

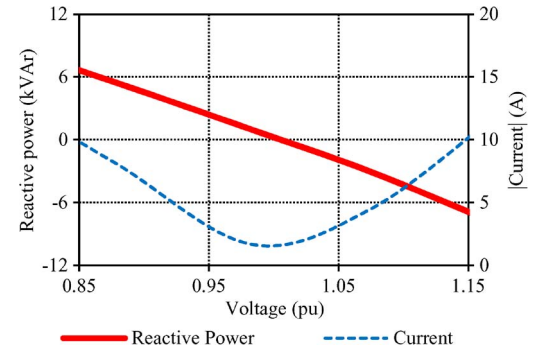


Fig. 19. Measured reactive power and line current versus per-unit terminal voltage (230 V = 1 pu voltage) at zero load.

draw reactive power. If the PMSG is designed in this way, the reactive power flow can be kept to a minimum. This however depends on the grid specifications. Capacitors can be also used at higher load values to correct the power factor. For a limited margin of the reactive power control, use can be made of tap-changing transformers.

VIII. CONCLUSION

In this paper, it has been shown that many of the constructional difficulties previously associated with PMIG type systems are alleviated by making use of the new concept SS-PMG. For the SS-PMG, nonoverlap windings can be used for both the S-PMG and PMSG units. This enables the design of a PM generator with a simple construction with low torque ripple. The construction of the SL-S-PMG is particularly simple with the use of preformed solid bar coils.

A simulation method has been developed whereby the SS-PMG can be optimally designed by using a few static solutions per iteration. This simplified method allows for significantly faster FE solution times. The results obtained by making use of the S-FE method are also shown to coincide well with T-FE analyses and practical measurements.

For the optimally FE designed SS-PMG, a very high overall efficiency of 92% is predicted at a slip value of about 2%. Even for the practically tested SS-PMG with the S-PMG units not optimally constructed, efficiencies comparable with other wind generator systems are observed. By specifying a higher rated slip value or thus lower rated efficiency, the mass of the S-PMG can be decreased in the design optimization.

The focus of the design optimization was to maximize the S-PMG's torque for a specific copper loss, which is the same as maximizing the efficiency of this generator. However, the focus of the design optimization can be also shifted to, for instance, the maximization of the pullout torque if a generator with a high pullout torque is required, or the focus can be the reduction of the mass of the generator. The pullout torque of the prototype SS-PMG unit is measured at 1.3 pu. For the prototype SS-PMG, the PMSG comprises 60.3% of the total mass of the generator, and the S-PMG (with copper windings) comprises about 39.7% of the mass. This mass ratio, however, can be improved by using, for example, aluminum S-PMG rotor bars. With a lower required pullout torque and efficiency, the mass can be reduced to an even further extent. It should be also noted that the total tower-top mass increase by adding the S-PMG is 23% for the prototype SS-PMG wind turbine system.

It is also shown that saturation and cross magnetization have a significant effect on the dq -inductances and the developed torque of the surface-mounted S-PMG and PMSG. Furthermore, it is shown that the SS-PMG automatically compensates for grid voltage variations, with reactive power control possible by using tap-changing transformers. The reactive power flow for different generator loads can be limited by changing the induced voltage of the generator in the design at rated speed or by using switch-in capacitors.

REFERENCES

- [1] F. Punga and L. Schon, "Der neue kollektorlose einphasenmotor der Firma Krupp," *Elektrotech. Zeitschrift*, vol. 47, no. 29, pp. 877–881, 1926.
- [2] J. F. H. Douglas, "Characteristics of induction motors with permanent-magnet excitation," *Trans. AIEE, Power App. Syst.*, vol. 78, no. 3, pp. 221–225, Apr. 1959.
- [3] J. K. Sedivy, "Induction motor with free-rotating DC excitation," *IEEE Trans. Power App. Syst.*, vol. PAS-86, no. 4, pp. 463–469, Apr. 1967.
- [4] W. F. Low and N. Schofield, "Design of a permanent magnet excited induction generator," in *Proc. ICEM*, 1992, vol. 3, pp. 1077–1081.
- [5] T. Epskamp, B. Hagenkort, T. Hartkopf, and S. Jockel, "No gearing, no converter: Assessing the idea of highly reliable permanent-magnet induction generators," in *Proc. EWEC*, 1999, pp. 813–816.
- [6] B. Hagenkort, T. Hartkopf, A. Binder, and S. Jöckel, "Modelling a direct drive permanent magnet induction machine," in *Proc. ICEM*, 2000, pp. 1495–1499.
- [7] G. Gail, T. Hartkopf, E. Tröster, M. Höffling, M. Henschel, and H. Schneider, "Static and dynamic measurements of a permanent magnet induction generator: Test results of a new wind generator concept," in *Proc. ICEM*, 2004, pp. 666–671.
- [8] E. Tröster, M. Sperling, and T. Hartkopf, "Finite element analysis of a permanent magnet induction machine," in *Proc. Int. SPEEDAM*, 2006, pp. 179–184.
- [9] Y. Shibata, N. Tsuchida, and K. Imai, "High torque induction motor with rotating magnets in the rotor," *Elect. Eng. Jpn.*, vol. 117, no. 3, pp. 102–109, 1996.
- [10] Y. Shibata, N. Tsuchida, and K. Imai, "Performance of induction motor with free-rotating magnets inside its rotor," *IEEE Trans. Ind. Electron.*, vol. 46, no. 3, pp. 646–652, Jun. 1999.
- [11] T. Fukami, K. Nakagawa, R. Hanaoka, S. Takata, and T. Miyamoto, "Nonlinear modeling of a permanent-magnet induction machine," *Elect. Eng. Jpn.*, vol. 144, no. 1, pp. 58–67, Jul. 2003.
- [12] T. Fukami, K. Nakagawa, Y. Kanamaru, and T. Miyamoto, "A technique for the steady-state analysis of a grid-connected permanent-magnet induction generator," *IEEE Trans. Energy Convers.*, vol. 19, no. 2, pp. 318–324, Jun. 2004.
- [13] T. Tsuda, T. Fukami, Y. Kanamaru, and T. Miyamoto, "Effects of the built-in permanent magnet rotor on the equivalent circuit parameters of a permanent magnet induction generator," *IEEE Trans. Energy Convers.*, vol. 22, no. 3, pp. 798–799, Sep. 2007.
- [14] A. J. Thomas, "A doubly-fed permanent magnet generator for wind turbines," M.S. thesis, MIT, Cambridge, MA, 2004.
- [15] R. Vermaak, J. H. J. Potgieter, and M. J. Kamper, "Grid-connected VSC-HVDC wind farm system and control using permanent magnet induction generators," in *Proc. IEEE Int. Conf. PEDS*, 2009, pp. 897–902.
- [16] A. J. G. Westlake, J. R. Bumby, and E. Spooner, "Damping the power-angle oscillations of a permanent-magnet synchronous generator with particular reference to wind turbine applications," *Proc. Inst. Elect. Eng.—Elect. Power Appl.*, vol. 143, no. 3, pp. 269–280, May 1996.
- [17] H. Müller, M. Pöller, A. Basteck, M. Tilshcher, and J. Pfister, "Grid compatibility of variable speed wind turbines with directly coupled synchronous generator and hydro-dynamically controlled gearbox," in *Proc. 6th Int. Workshop Largescale Integr. Wind Power Transm. Netw. Offshore Wind Farms*, 2006, pp. 307–315.
- [18] S. Grabic, N. Celanovic, and V. A. Katic, "Permanent magnet synchronous generator cascade for wind turbine application," *IEEE Trans. Power Electron.*, vol. 23, no. 3, pp. 1136–1142, May 2008.
- [19] D. A. Wills and M. J. Kamper, "Reducing PM eddy current rotor losses by partial magnet and rotor yoke segmentation," in *Proc. ICEM*, 2010, pp. 1–6.
- [20] D. A. Wills and M. J. Kamper, "Analytical prediction of rotor eddy current loss due to stator slotting in PM machines," in *Proc. ECCE*, 2010, pp. 992–995.
- [21] M. J. D. Powell, "An efficient method for finding the minimum of a function of several variables without calculating derivatives," *Comput. J.*, vol. 7, no. 2, pp. 155–162, 1964.
- [22] M. J. Kamper, F. S. Van der Merwe, and S. Williamson, "Direct finite element design optimisation of the cageless reluctance synchronous machine," *IEEE Trans. Energy Convers.*, vol. 11, no. 3, pp. 547–555, Sep. 1996.
- [23] J. H. J. Potgieter and M. J. Kamper, "Cogging torque sensitivity in design optimisation of low cost non-overlap winding PM wind generator," in *Proc. ICEM*, 2010, pp. 1–6.



computer-aided design.

Johannes H. J. Potgieter (S'10) was born in Oudtshoorn, South Africa, in March 1985. He received the B.Eng. and M.Sc. (Eng.) degrees in electrical and electronic engineering in 2008 and 2011, respectively, from the University of Stellenbosch, Stellenbosch, South Africa, where he is currently working toward the Ph.D. (Eng.) degree in the Department of Electrical and Electronic Engineering.

His current research focuses on wind power generation solutions and the optimizing of permanent-magnet machine technologies, including



Maarten J. Kamper (SM'08) received the M.Sc. (Eng.) degree in 1987 and the Ph.D. (Eng.) degree in 1996 from the University of Stellenbosch, Stellenbosch, South Africa.

Since 1989, he has been with the academic staff of the Department of Electrical and Electronic Engineering, University of Stellenbosch, where he is currently a Professor of electrical machines and drives. His research interests include computer-aided design and control of reluctance, permanent-magnet, and induction machine drives.

Prof. Kamper is a South African National Research Foundation Supported Scientist and a Registered Professional Engineer in South Africa.